RSC Advances

PAPER

View Article Online
View Journal | View Issue

Cite this: *RSC Adv.*, 2026, **16**, 26789

Fully plant-derived flaxseed mucilage-soy protein inks for extrusion-based 3D printing of tunable hydrogel scaffolds

Pooja Kumari, Rishabh Rai Kaushik, Snehlata Yadav and Sanjeev Kumar Mahto *

The development of sustainable, biocompatible bioinks is essential to advancing extrusion-based 3D printing. This study introduces a fully plant-derived ink system integrating flaxseed mucilage (FSM) and soy protein isolate (SPI) and systematically assesses its printability and scaffold performance. FSM was prepared at concentrations of 5%, 6%, and 7% (w/v), both independently and in combination with 4% SPI, followed by EDC-NHS crosslinking. Rheological analysis indicated a pronounced shear-thinning behavior across all formulations with increased FSM concentration and SPI incorporation; with the 7% FSM + 4% SPI blend exhibiting the highest consistency index (3684.31 Pa s), the lowest flow index (0.1605), and superior viscoelastic properties ($G' > G''$). Printability studies demonstrated improved filament fidelity and grid resolution with higher FSM content and SPI addition, with the 7% FSM + 4% SPI formulation exhibiting superior shape retention. Scanning electron microscopy (SEM) analysis confirmed the formation of interconnected porous architectures, while degradation studies in a phosphate-buffered saline (PBS) solution showed controlled structural erosion influenced by FSM concentration and SPI presence. FSM-only scaffolds exhibited high swelling capacity, which was substantially reduced upon SPI incorporation. Mechanical and thermal analyses demonstrated that SPI incorporation influenced scaffold stability and elasticity. Structural characterization through attenuated total reflectance Fourier transform infrared (ATR-FTIR) spectroscopy and X-ray diffraction (XRD) confirmed intermolecular interactions between FSM and SPI. Studies on the release of antibacterial drugs from ciprofloxacin-loaded scaffolds have shown concentration-dependent inhibition zones against *Bacillus subtilis*. Overall, this study demonstrates that FSM–SPI composite hydrogels offer tunable rheological, mechanical, and degradation properties, rendering them promising, sustainable inks for extrusion-based 3D printing applications.

Received 30th January 2026
Accepted 9th May 2026

DOI: 10.1039/d6ra00817h

rsc.li/rsc-advances

1 Introduction

The advancement of biocompatible, naturally sourced biomaterials has gained considerable interest in the fields of tissue engineering, wound care, and regenerative medicine.[1] Hydrogels and hydrogel-based scaffolds, in particular, exhibit adjustable mechanical properties, high water content, and structural similarity to the extracellular matrix (ECM), making them promising candidates for biomedical applications.[2] In recent years, extrusion-based 3D printing has emerged as a potent method for fabricating customizable scaffolds with precise geometries, controlled porosity, and reproducible architecture.[3,4] Nevertheless, the success of 3D printing is largely dependent on the formulation of printable inks that exhibit appropriate rheological behavior, mechanical stability, and structural integrity after printing.[4]

Natural polysaccharide-protein hydrogels have increased attention as sustainable inks for extrusion-based 3D printing due to their high water content, adjustable viscoelasticity, and inherent biocompatibility, which are suitable for soft-tissue engineering applications.[5] Flaxseed (*Linum usitatissimum*) mucilage, a hydrocolloid rich in heteropolysaccharides, exhibits significant shear-thinning, emulsifying, and water-retention properties, and has been explored for use in drug-delivery systems, food gels, and emerging tissue-engineering constructs.[6] Nonetheless, hydrogels composed solely of polysaccharides often demonstrate limited mechanical robustness and shape fidelity under printing conditions, necessitating strategies to reinforce the network or introduce additional interactions. Soy protein isolate (SPI), a widely available plant-based protein, exhibits excellent film-forming capabilities and functional groups that facilitate hydrogen bonding and covalent crosslinking.[7] Hydrogels based on or reinforced with SPI have shown enhanced mechanical properties and structural stability when combined with polysaccharides. Despite these advancements, limited research has systematically evaluated their synergistic potential for 3D printing applications. Specifically,

Tissue Engineering and Biomicrofluidics Laboratory, School of Biomedical Engineering, Indian Institute of Technology (Banaras Hindu University), Varanasi, Uttar Pradesh 221005, India. E-mail: skmahto.bme@iitbhu.ac.in

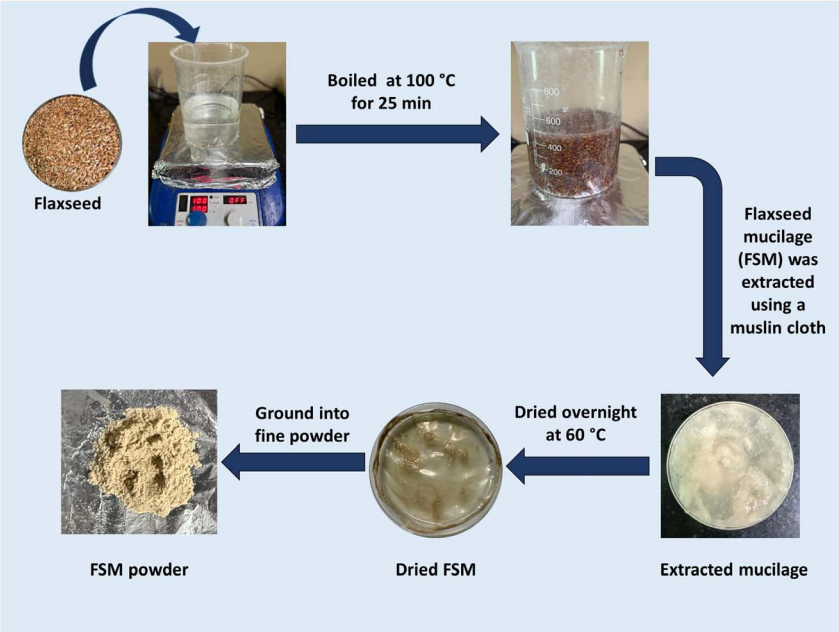

Fig. 1 Diagram illustrating the procedure for the preparation of flaxseed mucilage powder.

the impact of SPI incorporation on the rheology, structural organization, swelling behavior, mechanical strength, and printability of FSM remains insufficiently understood. Addressing this gap is crucial for establishing FSM–SPI as a sustainable, plant-based alternative to synthetic or animal-derived inks.

Therefore, this study aims to develop and characterize FSM and FSM–SPI-based inks for extrusion-based 3D printing, and to evaluate the influence of SPI incorporation on the rheological properties, printability, structural features, swelling behavior, mechanical performance, thermal stability, and crystallinity of the resulting scaffolds, with the broader goal of establishing a fully plant-derived ink.

2 Material method

2.1 Materials

Flaxseeds and muslin cloth were sourced from a local market in Varanasi, India. SPI powder was purchased from A. M. NUTRA TECH Pvt., Ltd, India. *N*-(3-dimethylaminopropyl) *N*′-ethyl-carbodiimide hydrochloride (EDC) (HiMedia, RM1817-25G), *N*-hydroxysuccinimide (NHS) (Sigma-Aldrich, 130672-25G), Luria–Bertani (LB) broth, 10 mL syringe with a Luer-Lok tip (BD, Ref-303064), phosphate-buffered solution (PBS) was purchased from HiMedia, India. Absolute ethanol (99.9%, high analytical grade) and distilled water were used in all experiments.

2.2 Preparation of mucilage powder from *Linum usitatissimum* L. (flaxseeds)

100 g of flaxseeds were accurately weighed and immersed in 400 mL of distilled water. The mixture was maintained at 100 °C for 25 min to facilitate mucilage extraction. After thermal treatment, the mucilage was separated from the seed residues using a muslin cloth. The extracted mucilage was then dried in a hot air oven at 60 °C for 24 h. Upon complete drying, the mucilage was ground into a fine powder using a mixer grinder and subsequently stored in airtight containers for further use (Fig. 1). The yield of flaxseed mucilage (FSM) (Y%) was calculated using eqn (1).

$$\text{Yield of flax seed mucilage}(Y\%) = \frac{W_{\text{fsm}}}{W_{\text{s}}} \times 100 \quad (1)$$

W_{fsm} – the weight of dried flaxseed mucilage; W_{s} – the weight of flaxseed used to extract the mucilage. The average from 4 samples was calculated.

2.3 Filament formation test

The filament formation test is a fundamental yet essential assessment of printability in biofabrication and 3D printing. It is used to evaluate whether a hydrogel can produce stable and continuous filaments suitable for scaffold fabrication. For the filament test, various concentrations of flaxseed mucilage powder (FSM) were mixed in distilled water (3%, 4%, 5%, 6%, and 7% FSM). The prepared inks were extruded manually, and those that formed stable, continuous filaments were selected for further preparation. The FSM ink, which formed a continuous filament, was combined with the 4% SPI to form the FSM–SPI-based ink.

2.4 Preparation of ink

The ink was prepared in different ratios, namely: 5% FSM (w/v), 5% FSM + 4% soya protein isolate (SPI) (w/v), 6% FSM (w/v), 6% FSM + 4% SPI (w/v), 7% FSM (w/v), and 7% FSM + 4% SPI (w/v). All formulations were prepared using distilled water as the

Table 1 Formulation of FSM alone and FSM–SPI ink samples with varying FSM concentrations

Ink (w/v)	SPI (g)	FSM powder (g)	Water (mL)
5% FSM	0	0.5	10
5% FSM + 4% SPI	0.4	0.5	10
6% FSM	0	0.6	10
6% FSM + 4% SPI	0.4	0.6	10
7% FSM	0	0.7	10
7% FSM + 4% SPI	0.4	0.7	10

solvent (Table 1). To prepare the FSM only, the required amount of FSM powder was accurately weighed and dispersed directly into 10 mL of distilled water under continuous stirring. For SPI-containing formulations, SPI was first dissolved in 10 mL of distilled water and stirred at 60 °C for 1 h to ensure complete dissolution. FSM powder was then added to the SPI solution and mixed thoroughly. Prior to printing, all ink material formulations were centrifuged to remove air bubbles and subsequently transferred into 10 mL syringes (Fig. 2 and S2–S9).

To prepare a cross-linking solution, EDC (25 mM) and NHS (12.5 mM) were dissolved in 90% ethanol. Before each experiment, this solution was prepared fresh and used to crosslink the printed scaffolds.

2.5 Rheology of the formulated ink blend

The rheological properties of the printing material significantly impact its performance during the 3D printing process, influencing its ability to be extruded, retain its shape, and respond to stress and strain.[8] The rheological properties of the inks were examined using the MCR 702e MultiDrive Rheometer from Anton Paar (Austria-Europe). This analysis employed a parallel-plate setup, with the upper plate having a 25 mm diameter and the lower plate a 50 mm diameter, separated by a 1 mm gap. Both a frequency sweep test and a rotational shear viscosity assessment were conducted on all selected inks. The frequency sweep test was carried out within the linear viscoelastic region of the inks to measure the storage modulus (G'), which reflects elasticity, and the loss modulus (G''), which indicates fluidity. Additionally, the loss factor (tan δ), representing the ratio of the loss modulus (G'') to the storage modulus (G'), was determined to quantify the material's viscoelastic balance. To further evaluate viscosity, a rotational shear viscosity test was conducted on the inks, with shear rates ranging from 0.1 to 100 s^{-1}. Subsequently, a graph of shear rate against viscosity was created, and the power law was applied using the appropriate formula (2).

$$\eta = K\gamma^{(n-1)} \quad (2)$$

In this context, K represents the consistency index, n denotes the flow index, both of which are shear-thinning coefficients, while γ stands for the shear rate, and η signifies the viscosity. The experiments were carried out at the same temperature used for printing, *i.e.*, 25–30 °C.

2.6 Printability, shape fidelity, and printing resolution of formulated ink blends

All the structures were created using a free platform, Tinkercad (https://www.tinkercad.com/). A detailed examination of ink resolution was conducted at various strand intervals. A square with a side length of 1.5 cm was produced with varying infill distances as directed by the printer (1, 2, 3, 4 mm). A hollow cube of 15 × 15 × 3 mm^3 with a grid infill distance of 8 mm

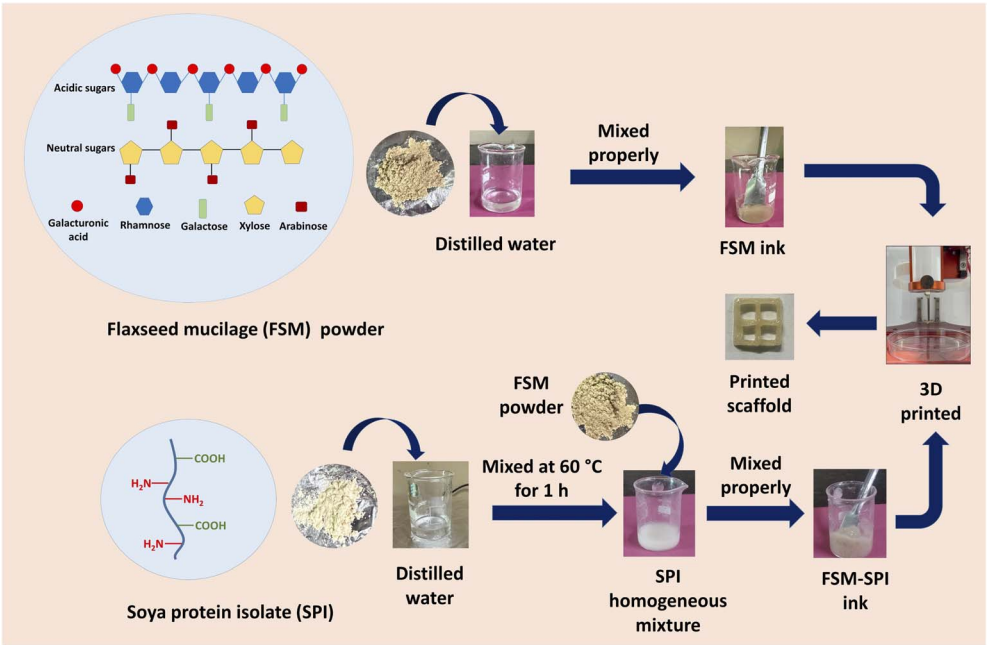

Fig. 2 Illustration depicting the methodology for fabricating a 3D-printed scaffold composed of flaxseed mucilage and soy protein isolate.

was 3D printed on a Petri dish using optimized printing parameters. The fabricated 3D scaffold was crosslinked with freshly prepared EDC-NHS and incubated at room temperature (RT) for 48 h. Post-incubation, the scaffolds were stored at −80 °C and lyophilized for subsequent experimental procedures.

To further evaluate 3D printing fidelity, two quantitative parameters were established: horizontal ductility and vertical sinking degree. The vertical sinking degree, indicative of the extent of vertical collapse or sagging of the printed filaments due to gravitational forces, was determined using eqn (3). The horizontal ductility refers to the extent of lateral spreading in relation to the designed dimension, as indicated by eqn (4).

$$\frac{\text{Actual height(Ah)}}{\text{Theoretical height(Th)}} = \text{vertical sinking degree} \quad (3)$$

$$\frac{\text{Actual area(Aa)}}{\text{Theoretical area (Ta)}} = \text{horizontal ductility} \quad (4)$$

2.7 Water uptake capacity

The water uptake capacity of the 3D-printed scaffold was assessed by immersing it in PBS (pH 7.4) at room temperature (RT) for 48 h. Samples were systematically weighed at regular intervals both before and after immersion, using a precision electronic balance. The samples were removed from the solution, gently blotted with tissue paper to eliminate excess surface moisture, and subsequently weighed. The swelling percentage was calculated using eqn (5).

$$\text{Swelling}(\%) = \left(\frac{W_a - W_b}{W_b}\right) \times 100 \quad (5)$$

where W_b is the scaffold weight before immersion, and W_a is the weight after immersion.

2.8 Structure characterization and degradation of the fabricated scaffolds

The surface morphology and pore structure of the 3D-printed scaffolds were examined using a scanning electron microscope (SEM). The scaffolds were coated with gold and imaged with a Jeol benchtop SEM (JCM-6000PLUS). For the degradation study, the scaffolds were immersed in PBS for 7 days, with the solution replaced every 3 days. Upon completion of this period, the samples were freeze-dried and subsequently visualized using SEM. The weight loss percentage after 7 days was calculated using eqn (6)

$$\left(\frac{W_i - W_f}{W_i}\right) \times 100 = \text{weight loss}(\%) \quad (6)$$

where W_i is the initial weight of the scaffold, and W_f is the final weight of the scaffold after 7 days.

2.9 Mechanical testing of the scaffolds

The scaffolds were freshly prepared, molded into solid cylindrical structures with a 13 mm diameter and 10 mm thickness, and then cross-linked for subsequent compression testing. The mechanical characteristics of these scaffolds were analyzed using a Brookfield CT3 texture analyzer, equipped with a 10 kg load cell. Compression tests were executed at a crosshead speed of 0.5 mm s^{-1} until the scaffolds reached 50% and 80% deformation (S10) at RT. To ensure the reliability of the results, all measurements were conducted in triplicate. Stress–strain curves were produced, and both the compressive strength and compressive modulus were calculated.

2.10 ATR-FTIR spectroscopy of the scaffolds

The ALPHA BRUKER Eco-ATR spectrometer, equipped with a ZnSe attenuated total reflection (ATR) accessory, was used to analyze the peaks and functional groups of the printed scaffolds. The analysis was performed with a resolution of 4 cm^{-1}, and each spectrum was obtained by recording 24 scans within the range of 500 to 4000 cm^{-1}.

2.11 X-ray diffraction analysis of the scaffolds

The X-ray diffraction (XRD) patterns of all scaffolds were obtained using a Bench Top X-ray Diffraction (BT XRD) system (Rigaku Miniflex 600 Desktop X-ray Diffraction System, RIGAKU Corporation). For XRD analysis, each scaffold was initially formed into a solid cylindrical shape with a 13 mm diameter and a 10 mm thickness. Following the crosslinking process, the cylinders were meticulously sectioned into thin sheets using a sterile surgical blade to ensure uniformity of the samples for analysis. Pure FSM powder and SPI powder were used directly for XRD analysis to examine their original peaks. The measurements were conducted at 40 kV and 15 mA, using Kα radiation ($\lambda = 1.54$ nm). The scanning was performed at a rate of 5 min per step within the 2θ range of 10° to 90°.

2.12 Thermal stability of the scaffolds

The thermal stability of the 3D-printed cross-linked scaffolds was evaluated using a TGA-50 thermogravimetric analyzer (Shimadzu (Asia Pacific) Pvt. Ltd). A 5 mg sample was placed in the instrument and heated at 10 °C min^{-1} to 20–1000 °C. TGA provides data on weight loss as a function of time, temperature, and environmental conditions, thereby facilitating the assessment of the material's thermal stability.

2.13 Drug release study

The antibacterial assay assessed the drug-release capability of the fabricated scaffolds using a disc diffusion test against *Bacillus subtilis* (ATCC 168). The bacterial cultures were maintained in Luria–Bertani (LB) broth (HiMedia, Mumbai). Following overnight incubation, the bacterial cultures were spread onto freshly prepared nutrient agar plates. For the antibacterial drug release study, the fabricated scaffolds, designated as 5% FSM, 6% FSM, 7% FSM, 5% FSM + 4% SPI, 6% SPI + 4% SPI, and 7% FSM + 4% SPI, along with Whatman filter paper serving as a control, were cut into disc shapes and sterilized using 70% ethanol, followed by ultraviolet radiation prior to the experiments. After sterilization, both scaffolds and the

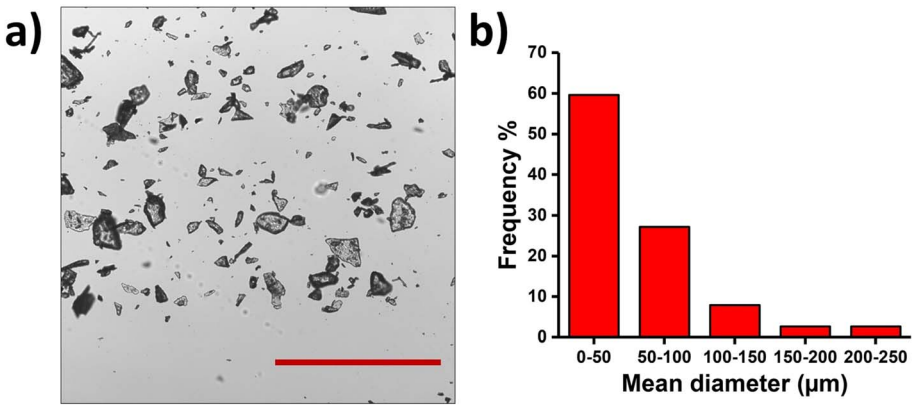

Fig. 3 (a) Represents the bright-field image of flaxseed mucilage powder. (b) Represents the bar graph of the frequency of particle size of the extracted powder scale bar: 500 μm.

control were immersed in a 1 mg mL^{-1} solution of ciprofloxacin hydrochloride hydrate for 15 min. Subsequently, they were placed on agar plates and incubated for 24 h at 37 °C. The zones of inhibition were documented using a digital camera after the 24 h incubation period.

2.14 Statistical analysis

Data analysis was conducted utilizing OriginPro software. Quantitative outcomes are presented as the mean ± standard deviation (SD), derived from triplicate measurements for each experimental condition.

3 Results

3.1 Yield of flaxseed mucilage

The flaxseed mucilage (FSM) was isolated through aqueous extraction, followed by drying at 60 °C. The yield of the extracted mucilage was determined to be 5.45 ± 0.53%, aligning with previously reported values ranging from 3.5% to 12.7% of the total seed weight. The ground FSM powder was further characterized using bright-field microscopy to assess particle size distribution (Fig. 3a). The majority of particles (59.65%) were observed within the 0–50 μm range, followed by 27.19% in the 50–100 μm range, with only 13.15% of particles exceeding 100 μm in diameter (Fig. 3b). These findings suggest that FSM powder predominantly consists of fine particles, a characteristic anticipated to enhance its solubility, dispersion, and functional performance in scaffold fabrication and related biomedical applications (S1).

3.2 Filament formation test

The filament formation assay was conducted as a preliminary step to select a suitable hydrogel ink for extrusion-based 3D printing. Hydrogel inks that demonstrated continuous and unbreakable release were selected. Initially, a lower concentration (3% or 4%) of FSM-hydrogel ink was loaded into a 10 mL

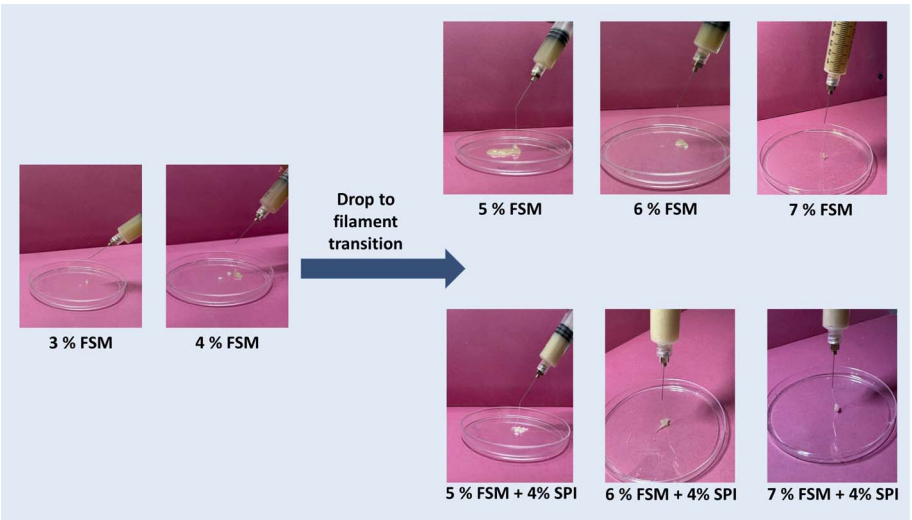

Fig. 4 Depicting the filament formation assay of FSM inks, both with and without the addition of SPI. The images illustrate the extrusion behavior at varying FSM concentrations (3%, 4%, 5%, 6%, and 7%) and their respective mixtures with 4% SPI of the selected ink.

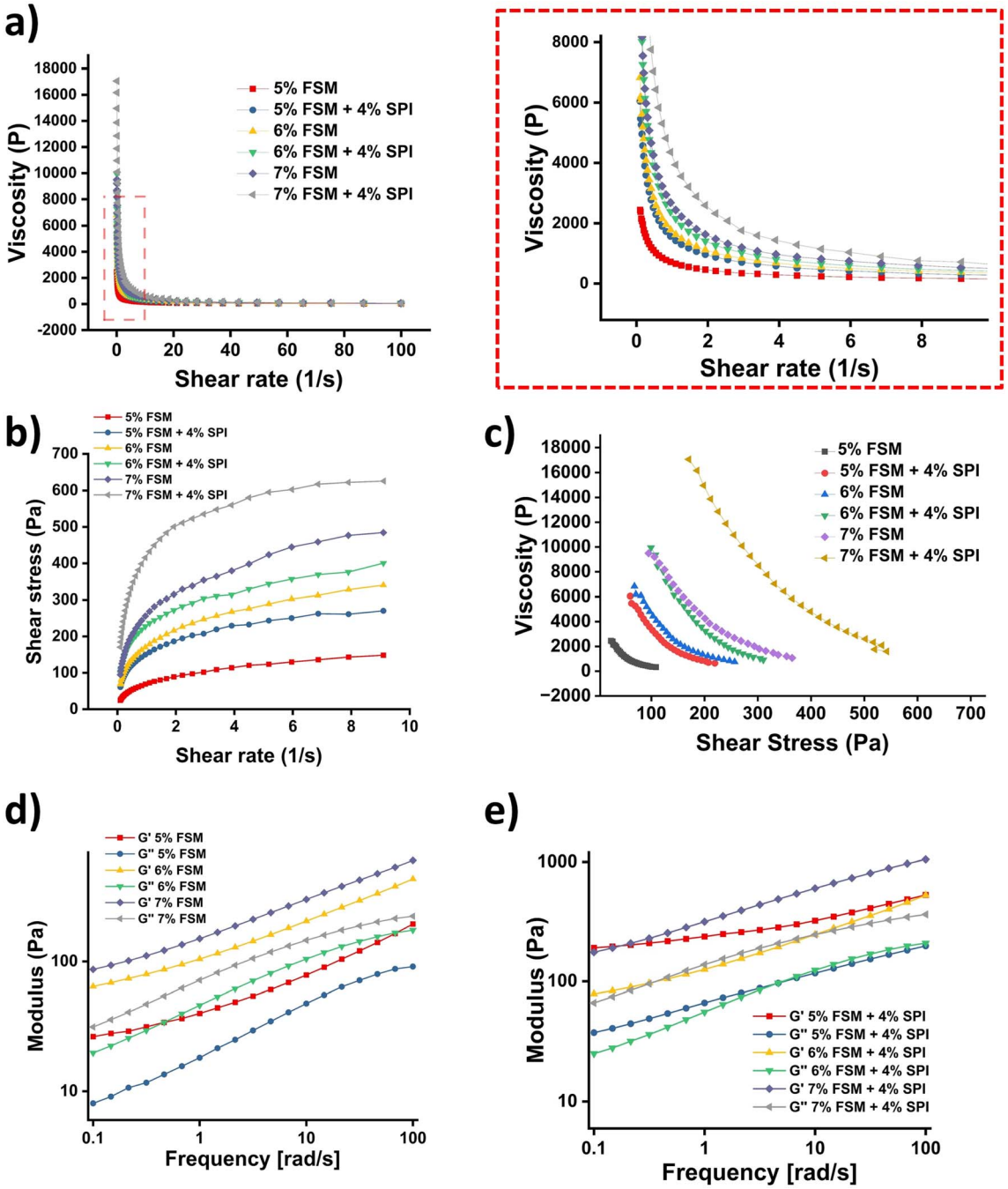

Fig. 5 Rheological properties of the inks. Plots between: (a) viscosity and shear rate plot and its corresponding zoomed view, (b) shear stress *vs.* shear rate, (c) viscosity *vs.* shear stress, (d) modulus *vs.* frequency for FSM alone ink sample, (e) modulus *vs.* frequency of FSM + SPI ink blend sample.

Luer-Lock syringe fitted with a 25 *G* needle. When the formulated ink was mechanically extruded, it formed droplet-like structures, indicating weak structural integrity and leading to poor filament formation and discontinuous extrusion. Increasing the ink concentration to 5% FSM resulted in the formation of a continuous filament, indicating improved printability. Further enhancement was observed with 6% and 7% FSM, where the extruded filaments maintained their shape without immediate breakage or spreading. In further assessments, 4% SPI was incorporated into selected inks (5%, 6%, and 7%) to evaluate filament formation. The results indicated that the ink exhibited improved filament stability, characterized by uniform extrusion and a reduction in filament breakage (Fig. 4 and S2–S9).

3.3 Rheology of the formulated ink blend

The rheological characterization of inks was conducted to assess their viscoelastic properties and flow behavior. Based on

Table 2 Various inks formulation and their consistency index (K), flow index (n), tan δ, and yield stress values

Concentration	Consistency index (K) (Pa s)	Flow index (n)	tan δ	Yield stress (Pa)
5% FSM	660.09	0.3391	0.55	24.47
5% FSM + 4% SPI	1415.93	0.2706	0.48	60.45
6% FSM	1637.71	0.2765	0.45	68.31
6% FSM + 4% SPI	2144.33	0.2382	0.44	99.42
7% FSM	2375.89	0.2622	0.39	94.92
7% FSM + 4% SPI	3684.31	0.1605	0.35	170.46

these properties, we aimed to evaluate their suitability for extrusion-based 3D printing. All formulations exhibited shear-thinning behavior, as indicated by the decrease in viscosity with increasing shear rate, which is favorable for smooth extrusion (Fig. 5a). The incorporation of SPI increased viscosity compared to FSM alone, with the 7% FSM + 4% SPI formulation showing the highest viscosity. Similarly, shear stress increased with concentration and SPI addition (Fig. 5b). The pattern of shear stress is as follows: 7% FSM + 4% SPI > 7% FSM > 6% FSM + 4% SPI > 6% FSM > 5% FSM + 4% SPI > 5% FSM. Flow initiation analysis (Fig. 5c) indicated that higher concentrations and SPI incorporation required greater stress to initiate flow, reflecting increased resistance to deformation. Power law analysis further supported these findings, showing that FSM–SPI inks exhibited a higher consistency index (K) and a lower flow index (n) than FSM alone (Table 2). The 7% FSM + 4% SPI formulation showed the highest K and lowest n values, indicating enhanced viscosity and more pronounced shear-thinning behavior.

Frequency sweep analysis provides further insights into the viscoelastic properties of the inks. As illustrated in Fig. 5d and e, the storage modulus (G'), which reflects the material's solid-like, elastic characteristics, consistently surpasses the loss modulus (G''), indicative of its liquid-like, viscous properties, across all formulations and frequencies. This finding implies a predominantly solid-like behavior. The moduli of all formulations demonstrate a positive correlation with frequency, with the 7% FSM–SPI ink exhibiting the highest values for both G' and G'', suggesting a denser, more robust gel network due to its higher concentration. The tan δ (tan $\delta = G''/G'$) values were also evaluated to quantify the ratio of viscous to elastic behavior. The hierarchy of tan δ values confirms that the presence of SPI in conjunction with FSM, as well as higher concentrations of FSM–SPI ink, results in a more solid-like, structurally stable material, which is crucial for achieving stable, layer-by-layer deposition during printing.

3.4 Printability, shape fidelity, and printing resolution of formulated ink blends

All the scaffolds were printed using an Allevi 2 extrusion-based 3D bioprinter using the optimized parameters (Table 3). For printing, the formulated inks were loaded into a 10 mL syringe (BD Biosciences) attached with a 25 G needle. The printing resolution was assessed by printing each ink at varying inter-strand distances (1, 2, 3, 4 mm). At a lower FSM concentration of 5%, the printed constructs exhibited poor shape fidelity at a 1 mm spacing, characterized by considerable line spreading and merging. However, an enhanced grid definition was observed at 3 and 4 mm spacings. Increasing the FSM concentration to 6% and 7% further improved printing resolution, yielding more distinct grid patterns and better pore definition, especially at larger spacings. The addition of 4% SPI further augmented the structural integrity of the printed scaffolds, reducing spreading and maintaining well-defined filaments even at a 1 mm spacing. Among all formulations, the combination of 7% FSM and 4% SPI exhibited the highest printing resolution and shape fidelity across all spacings, demonstrating superior printability and structural stability (Fig. 6). These findings suggest that increasing the polymer concentration and incorporating protein components significantly enhance the resolution and fidelity of extrusion-based printed constructs. A square structure with dimensions of 15 × 15 × 3 mm and an infill distance of 8 mm was fabricated to enable subsequent characterizations, as depicted in Fig. 7.

Further the horizontal ductility values were determined as follows: 5% FSM (0.37 ± 0.007), 6% FSM (0.44 ± 0.01), 7% FSM (0.58 ± 0.004), 5% FSM + 4% SPI (0.49 ± 0.03), 6% FSM + 4% SPI (0.58 ± 0.01), and 7% FSM + 4% SPI (0.67 ± 0.002). Notably, the FSM + SPI formulations consistently exhibited higher horizontal ductility compared to their corresponding FSM-only groups, indicating improved filament continuity and enhanced printing resolution. Among all groups, the 7% FSM + 4% SPI formulation demonstrated the highest horizontal ductility. The vertical sinking degree values were documented as follows: 5% FSM (0.95 ± 0.01), 6% FSM (1.04 ± 0.01), 7% FSM (1.11 ± 0.02), 5% FSM + 4% SPI (1.09 ± 0.01), 6% FSM + 4% SPI (1.05 ± 0.02), and 7% FSM + 4% SPI (1.01 ± 0.007). An optimal value is one that approaches 1, indicating greater shape fidelity

Table 3 Optimized printing parameters for FSM alone and FSM + SPI-based inks

Printing parameter	5% FSM	6% FSM	7% FSM	5% FSM + 4% SPI	6% FSM + 4% SPI	7% FSM + 4% SPI
Temperature (°C)	25–30	25–30	25–30	25–30	25–30	25–30
Needle sizes (Gauge)	25 G	25 G	25 G	25 G	25 G	25 G
Layer height (mm)	0.3	0.3	0.25	0.3	0.3	0.25
Pressure (Psi)	40	65	75	70	85	94
Print speed (mm s^{-1})	6	6	5	6	6	5
Grid infill distance	8	8	8	8	8	8

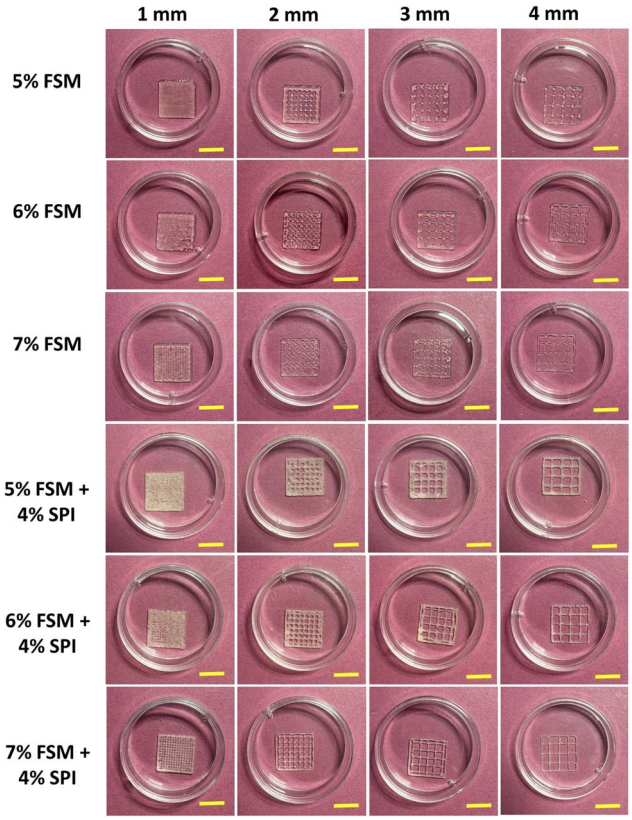

Fig. 6 The figure illustrates the impact of varying FSM concentrations and the incorporation of SPI on printing resolution across different inter-strand distances (1, 2, 3, and 4 mm) scale bar 1 cm.

and minimal deformation after printing. Slight deviations above 1 can be attributed to the ink's resistance to deformation during extrusion. Significantly, the 7% FSM + 4% SPI formulation achieved a value closest to 1, indicating superior structural integrity and shape retention (Fig. 8). These quantitative results demonstrate that the formulation with 7% FSM and 4% SPI offers the most effective combination of printing resolution, filament stability, and shape fidelity.

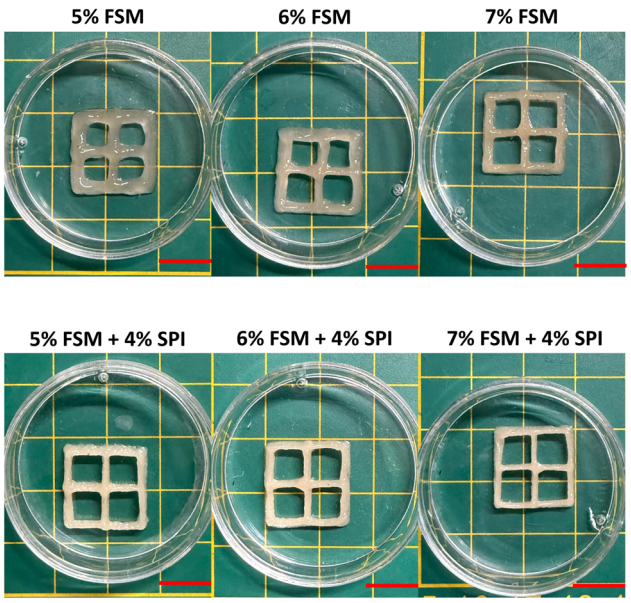

Fig. 7 Digital image of a 3D printed scaffold using various ink compositions scale bar 1 cm.

3.5 Water uptake capacity and degradation of the fabricated scaffold

The water uptake capacity of all cross-linked 3D-printed structures was assessed by immersing the printed scaffold in PBS for 48 h. All the scaffolds showed a rapid increase in swelling within 4 h, followed by gradual stabilization. The flaxseed mucilage alone scaffolds showed greater PBS absorption than those prepared with a flaxseed-SPI blend. The swelling ratio of the scaffold was recorded as follows: 5% FSM-3000.79 $\pm$ 84.27, 6% FSM-2709.11 $\pm$ 180.04, 7% FSM-2665.37 $\pm$ 117.46, 5% FSM + 4% SPI-1259.5 $\pm$ 155.49, 6% FSM + 4% SPI-1138.49 $\pm$ 99.91, and 7% FSM + 4% SPI-1088.2 $\pm$ 146.43. The elevated swelling observed in pure FSM hydrogels is consistent with the polysaccharide composition of FSM, which is highly hydrophilic and capable of absorbing substantial quantities of water. The reduction in swelling ratio with increasing FSM concentration (5% > 6% > 7%) may be attributed to the increased polymer density, which limits the availability of free volume for water uptake at higher concentrations (Fig. 9). The incorporation of 4% SPI markedly reduces the swelling capacity. This is likely due to SPI facilitating additional protein-polymer interactions, resulting in a denser, more cross-linked network that restricts water diffusion and homogenizes the structure. SPI functions as a stabilizing agent, enhancing mechanical integrity while reducing excessive swelling.

3.6 Structure characterization and degradation of the fabricated scaffolds

SEM micrographs of FSM-based scaffolds with and without SPI incorporation are represented in Fig. 10. All samples presented a three-dimensional network of porosity, which is essential for nutrient diffusion, fluid uptake, and cell infiltration. However, remarkable differences in pore size distribution and structural integrity were identified depending on the FSM concentration and the addition of SPI. For the lower FSM concentration of 5%, the formation of larger and irregular pores with relatively smooth, sheet-like walls and some areas with collapsed regions was identified. The freeze-drying of the mucilage results in a foam-like morphology, consisting mainly of polysaccharide lamellae. Increasing the FSM concentration from 6% to 7% resulted in a denser structure, with thicker walls and more interconnected, but smaller, pores. This may indicate increased viscosity upon gelation and also increased intermolecular interactions, which result in a compact polymeric network. All formulations with FSM + 4% SPI showed a more uniform pore-size distribution, with rougher, thicker walls; this indicates increased structural integrity and, therefore, stronger intermolecular interactions between SPI and FSM during gelation and freeze-drying. The presence of SPI likely served as a reinforcing agent, enhancing the matrix's structural organization.

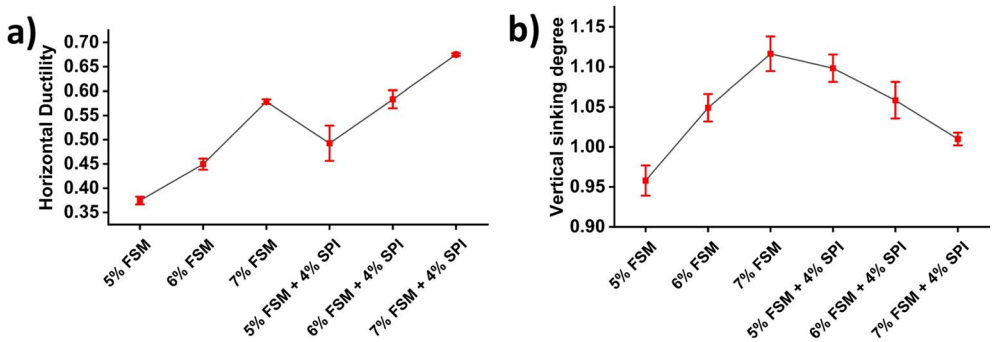

Fig. 8 Quantitative evaluation of print fidelity of FSM and FSM–SPI inks: (a) horizontal ductility and (b) vertical sinking degree for various formulations. Data are presented as mean ± SD ($n = 3$).

The scanning electron microscopy (SEM) micrographs demonstrate that both the concentration of FSM and the incorporation of SPI significantly affect the degradation and structural integrity of the scaffolds after seven days in PBS (Fig. 11a). At 5% FSM, the structure appears highly collapsed, with a low number of well-defined pores. This suggests a substantial loss of the original porous network, potentially due to swelling-induced collapse during degradation. At 6% FSM, a more recognizable layered morphology is observed, with some larger voids still visible, indicating slightly enhanced structural stability despite ongoing erosion of pore walls. At 7% FSM, the matrix appears the most compact and intact among the FSM-only samples, exhibiting fewer open voids and a smoother, denser surface. This is consistent with slower degradation and a higher crosslink density at increased FSM content. In a 5% FSM + 4% SPI scaffold, a more open, interconnected, and porous network is visible compared to 5% FSM alone, with thinner walls and extensive micro-porosity. This indicates that SPI introduces additional phase domains, thereby accelerating surface and bulk erosion. 6% FSM + 4% SPI large, well-defined macropores coexist with abundant micropores, suggesting that partial removal of SPI-rich regions during PBS incubation results in a highly porous, sponge-like architecture that is beneficial for fluid transport but reflects substantial mass loss. In 7% FSM + 4% SPI, the structure is highly tortuous, with rounded pores and rough internal surfaces, suggesting that the denser FSM matrix resists complete collapse, while SPI leaching and hydrolysis generate a heterogeneous porous network. Increasing FSM concentration from 5% to 7% slowed the degradation process, preserving the architecture and enhancing network stability. The addition of 4% SPI results in increased pore formation and heterogeneity across all FSM levels. This is consistent with the preferential dissolution or degradation of protein domains, which enhances porosity but also results in greater mass loss than in FSM-only counterparts.

These observations were quantitatively supported by weight loss analysis (Fig. 11b). Scaffolds composed of FSM alone exhibited relatively low degradation, with weight losses % of approximately 9.47 ± 1.96 (5% FSM), 7.55 ± 0.77 (6% FSM), and 7.32 ± 1.6 (7% FSM). Conversely, scaffolds incorporating SPI demonstrated significantly higher degradation, with weight loss increasing to 18.25 ± 1.58 (5% FSM + 4% SPI), 30.81 ± 3.36 (6% FSM + 4% SPI), and 34.46 ± 3.73 (7% FSM + 4% SPI). This enhanced degradation is attributed to the preferential dissolution of SPI-rich domains, which promotes increased mass loss and structural breakdown.

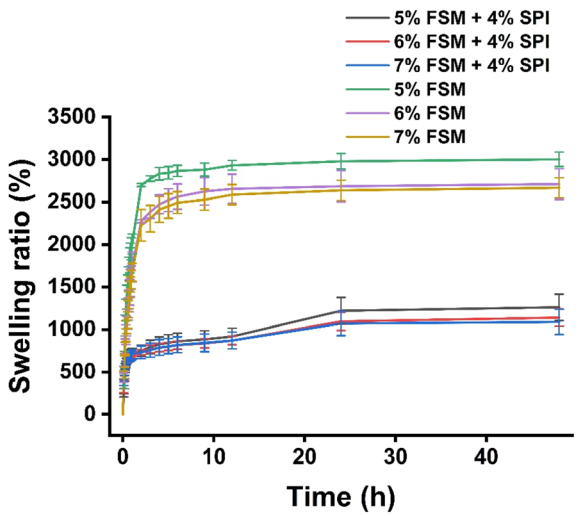

Fig. 9 Illustrates the swelling ratio (%) of FSM and FSM–SPI composite scaffolds of different compositions for over 48 h.

3.7 Mechanical testing of the scaffolds

Assessment of mechanical properties is critical for ensuring the stability of the resultant biomaterial constructs. As illustrated in the Fig. 12a, the mechanical properties were evaluated using uniaxial compression testing, where FSM and FSM + SPI scaffolds were subjected to 50% deformation, and recovery of shape was observed, indicating their elastic behavior. Further nonlinear stress–strain curves of the FSM and FSM + SPI scaffolds are illustrated in the Fig. 12b, representing the FSM scaffolds as expressing a superior stress response throughout the strain range compared to the FSM + SPI scaffolds. As illustrated in Fig. 12c, the maximum uniaxial stress sustained at 50% deformation by FSM scaffolds was approximately found to be 8.04 ± 0.28 kPa for 5% FSM, 11.38 ± 2.11 kPa for 6% FSM, and 11.63 ±

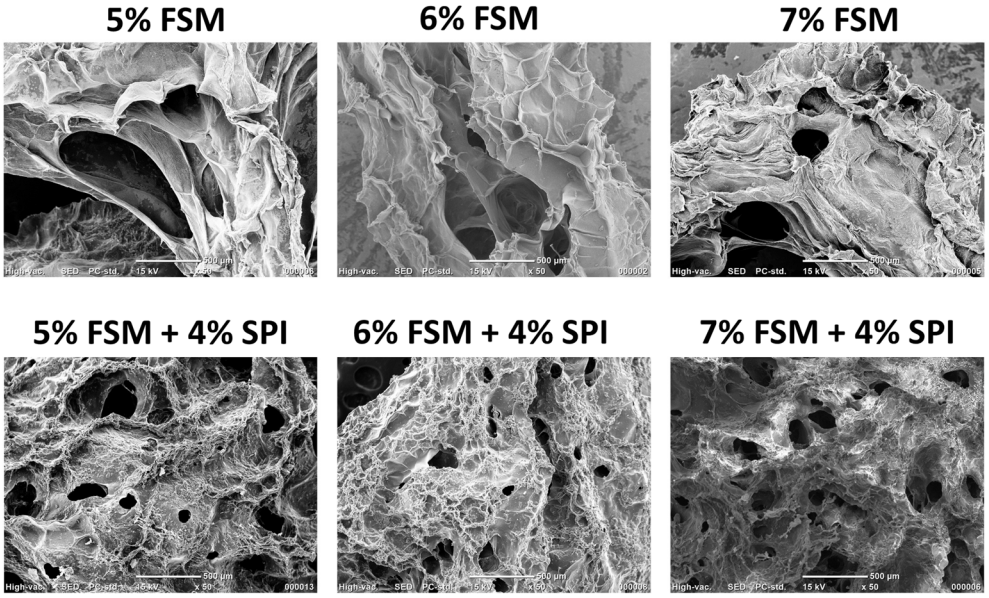

Fig. 10 SEM micrograph of FSM alone and FSM incorporated SPI scaffolds.

0.45 kPa for 7% FSM, whereas FSM + SPI scaffolds showed values of 5.40 ± 0.66 kPa for 5% FSM + 4% SPI, 8.11 ± 1.76 kPa for 6% FSM + 4% SPI, and 12.43 ± 3.30 kPa for 7% FSM + 4% SPI. Likewise, the compressive modulus of scaffolds illustrated in the Fig. 12d was approximately found to be 16.14 ± 0.57 kPa for 5% FSM, 22.84 ± 4.24 kPa for 6% FSM, and 23.35 ± 0.91 kPa for 7% FSM, while the corresponding values for FSM + SPI scaffolds were 10.86 ± 1.31 kPa for 5% FSM + 4% SPI, 16.41 ± 3.79 kPa for 6% FSM + 4% SPI, and 24.96 ± 6.63 kPa for 7% FSM + 4% SPI.

3.8 ATR-FTIR spectroscopy of the fabricated scaffolds

The FTIR spectra in Fig. 13 show the profiles of pure FSM at 5%, 6%, and 7% concentrations, as well as those of composites incorporating SPI (FSM + 4% SPI). Each formulation exhibited distinct absorption bands characteristic of polysaccharides, thereby verifying the presence of functional groups linked to flaxseed mucilage. A broad absorption band, spanning 3200–3400 cm^{-1}, was consistently observed across all samples, indicating the presence of O–H stretching vibrations of polysaccharides.[9] This suggests significant hydrogen bonding and highlights the hydrophilic nature of the mucilage matrix. Furthermore, a peak detected near 2920–2940 cm^{-1} corresponds to the C–H stretching of aliphatic groups present in sugar moieties.[10] In pure FSM samples, the prominent bands observed around 1600 cm^{-1} are attributed to the C=O stretching of carboxylate or amide groups, thereby confirming the presence of uronic acid residues.[4,5] Additionally, a distinct band near 1400 cm^{-1} corresponds to the C–OH group of uronic acid. Furthermore, absorption bands between 1000–1100 cm^{-1} indicate C–O–C and C–OH stretching vibrations, which are characteristic of glycosidic linkages in polysaccharides.[11] Upon the incorporation of 4% SPI, notable spectral shifts and alterations in peak intensity were observed. In particular, the broad O–H/N–H stretching band shifted to lower wavenumbers, from about 3310 cm^{-1} in FSM to 3279 cm^{-1} in the SPI-containing samples (Fig. 13b). In addition, samples containing SPI showed a peak at 1629 cm^{-1}, corresponding to amide I (C=O stretching), while a peak around 1521 cm^{-1} was associated with amide II (N–H bending).[12] A small peak shift and broadening in the band near 1408 to 1401 were also observed (Fig. 13c). These observations suggest the successful integration of protein molecules into the mucilage matrix. The changes support the presence of intermolecular hydrogen bonding between the carboxyl and hydroxyl groups of FSM and the amino groups of SPI.

3.9 X-ray diffraction analysis of the fabricated scaffolds

X-ray diffraction (XRD) analysis is frequently employed to evaluate the formation of crystal structures. In this study, XRD was utilized to investigate the structural effects arising from the interaction between SPI and FSM. The XRD pattern of pure FSM, SPI powder, and the scaffolds fabricated using FSM alone and with SPI is presented in Fig. 14. The X-ray diffractograms for all samples exhibited characteristics typical of amorphous materials, with no sharp peaks. The XRD pattern of pure FSM displayed only a single peak at $2\theta = 19.2°$, characteristic of an amorphous phase.[13] Soy protein isolate (SPI) exhibited two prominent diffraction peaks at $2\theta = 8.9°$ and 19.2°, which are indicative of the α-helix and β-sheet structures, respectively, within the secondary conformation of the soy protein molecule.[14]

The X-ray diffractogram for all concentrations of FSM alone exhibits characteristics typical of amorphous materials, lacking any sharp peaks. In the carbohydrate-based flaxseed gum, the prevalence of hydroxyl (OH) groups facilitated the formation of both intra- and intermolecular hydrogen bonds. This, in turn, resulted in varying degrees of junction coherence and an amorphous transformation.[13] All scaffolds showed a relatively broad peak at $2\theta \approx 16.08°$ and 24.6° for flaxseed mucilage. The shift in

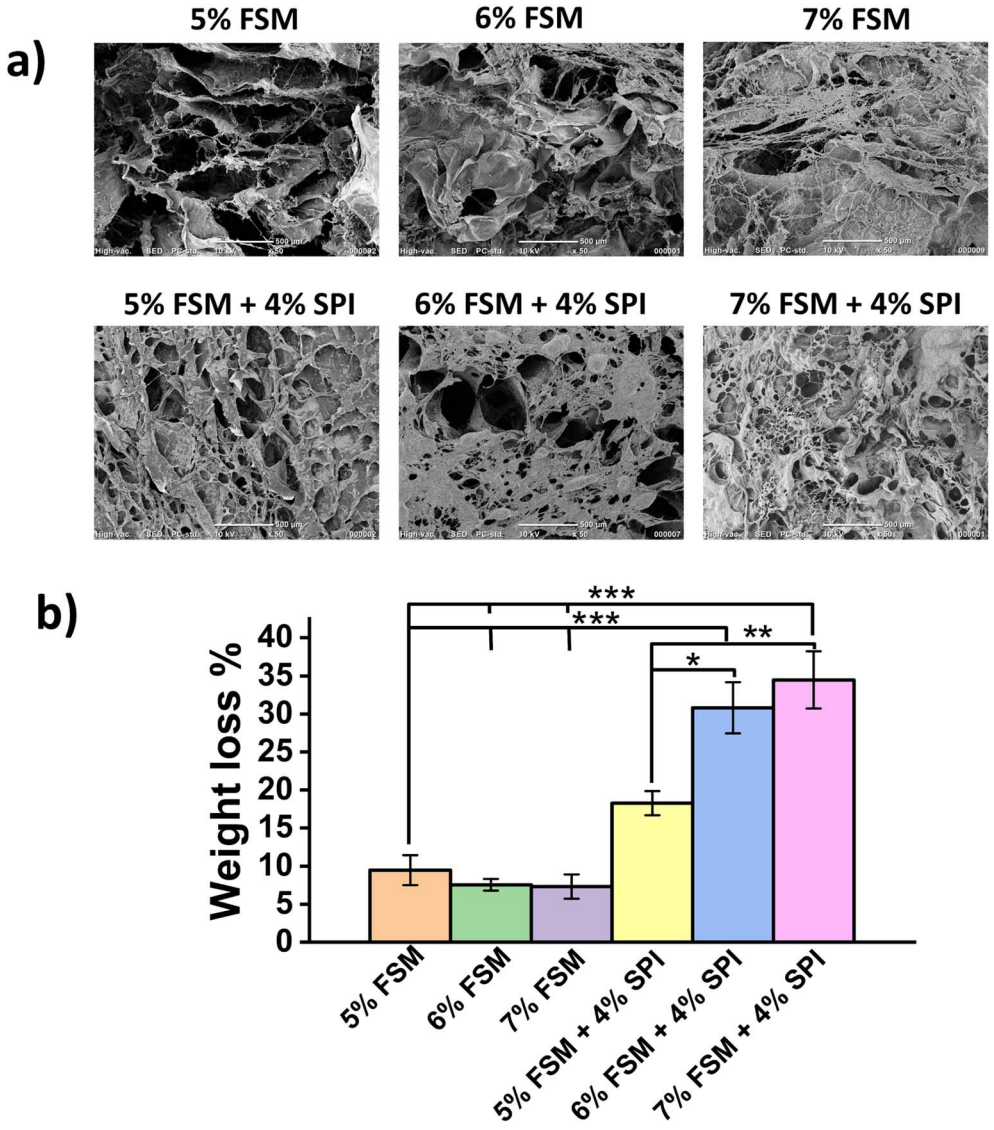

Fig. 11 Degradation study of FSM alone and FSM incorporated SPI scaffolds after 7 days in PBS; (a) SEM micrograph depicting the morphological changes that occurred after 7 days of incubation in PBS, (b) quantitative analysis of degradation represented as percentage weight loss after 7 days. Data are presented as mean ± standard deviation ($n = 3$), with statistical significance denoted as ***$p < 0.001$.

2θ from 19.2° to 16.15° may be attributed to the semi-organized packing of polysaccharide chains, including the local ordering of sugar rings and hydrogen-bonded domains that occurred due to crosslinking. Flaxseed mucilage primarily functions as an amorphous hydrocolloid, with high swelling and flexible hydrogel behavior, as opposed to rigid crystalline domains. The addition of 4% SPI to FSM enhances the intensity of the existing peaks and introduces a new small peak at 13.13°, indicating the formation of more ordered micro-domains and specific protein–polysaccharide interactions, rather than a fully crystalline phase. When SPI is blended with polysaccharides, XRD peaks often become sharper or more intense, reflecting denser chain packing and partial ordering due to hydrogen bonding and other intermolecular interactions between protein and polysaccharide chains. New low-angle peaks (around 13.3°) that appear after introducing a protein into a polysaccharide matrix are typically attributed to additional periodicities associated with protein secondary structures, such as ordered α-helices or β-sheets, or newly formed protein–polysaccharide complexes.

3.10 Thermal stability of the scaffolds

The thermal stability of the FSM alone and FSM with SPI, 3D printed scaffold, was evaluated to quantitatively determine the mass change profile as a function of temperature. The temperature-dependent weight change profile shown in Fig. 15a exhibits three distinct degradation stages. The primary degradation phase spanning from 30 to 200 °C is primarily correlated with the removal of residual moisture and sample dehydration, due to which the 5% FSM ink shows an approximate weight loss of 11.24%, 6% FSM shows 11.82% 7% FSM shows 10.82%, 5% FSM + 4% SPI shows 10.21%, 6% FSM + 4% SPI shows 9.55% and 7% FSM + 4% SPI shows 9.21% of weight loss. After the initial dehydration phase, the second phase corresponds to the

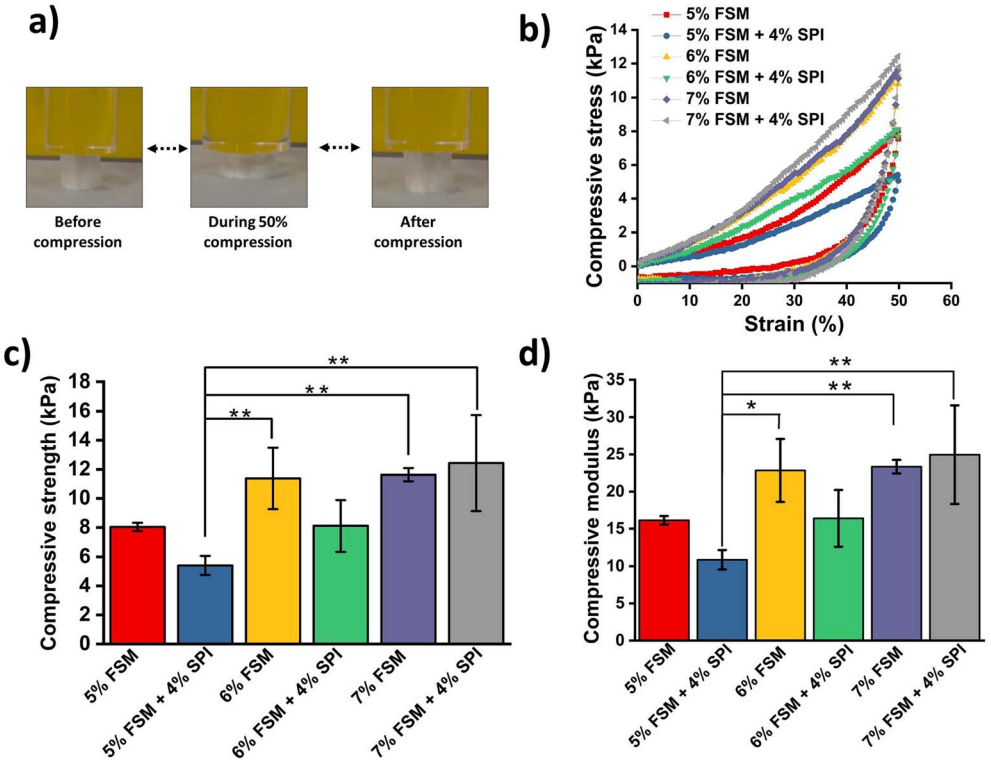

Fig. 12 Compressive mechanical evaluation of FSM and FSM + SPI-based scaffolds: (a) a visual representation of scaffold deformation under 50% uniaxial compression, illustrating the stages of pre-compression, during compression, and post-compression; (b) stress–strain curves depicting their compressive behavior with increasing strain; (c) a bar graph comparing the compressive strength (kPa) of the scaffolds; (d) compressive modulus (kPa) of the fabricated scaffolds. Data are presented as mean ± standard deviation ($n = 3$), with statistical significance denoted as $^{**}p < 0.01$.

breakdown of the core polymeric structure, spanning 200–380 °C. In this phase, the core molecular framework of the polymer gets cleaved, due to which 5% FSM ink shows an approximate weight loss of 50.85%, 6% FSM shows 48.43%, 7% FSM shows 48%, 5% FSM + 4% SPI shows 41.3%, 6% FSM + 4% SPI shows 45.21% and 7% FSM + 4% SPI shows 44.03% of weight loss. Thereafter, the final decomposition phase extends to 800 °C, during which the gradual degradation and carbonization occurred, leaving a residual mass. During this phase, the weight losses were determined to be 33.58% for 5% FSM, 34.7% for 6% FSM, 35.91% for 7% FSM, 38.03% for 5% FSM + 4% SPI, 38.54% for 6% FSM + 4% SPI, and 39.15% for 7% FSM + 4% SPI (Fig. 15b). From the TGA results, there are no significant differences between the FSM alone and the FMS + SPI-based scaffold.

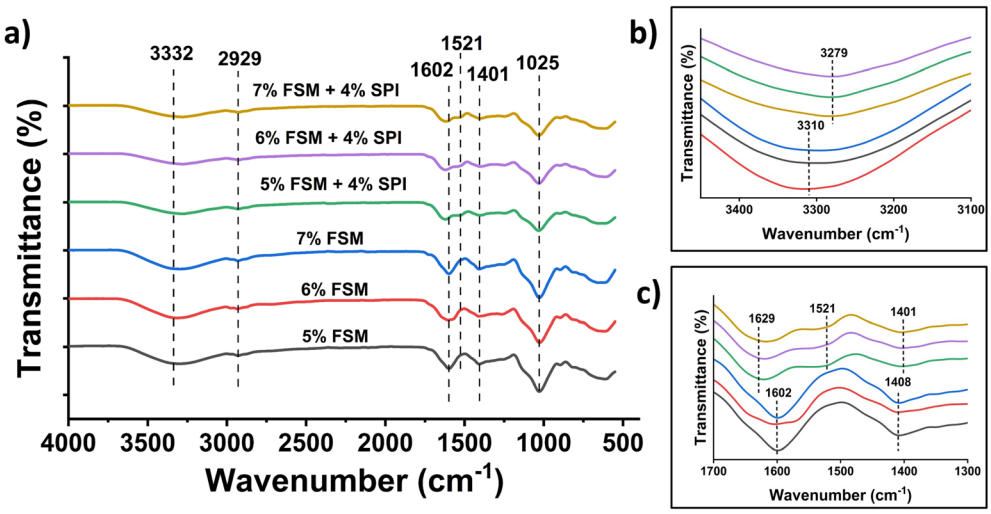

Fig. 13 Depicts the FTIR spectra of FSM alone (5%, 6%, 7%) and the composite scaffold (FSM + 4% SPI). (a) Full spectra (4000–500 cm^{-1}) of all cross-linked scaffolds (b) enlarged view of the 3400–3100 cm^{-1} region (c) enlarged view of the 1700–1300 cm^{-1} region.

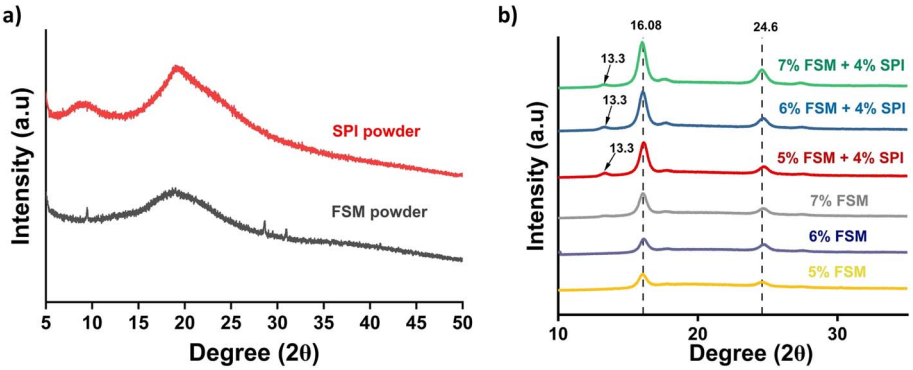

Fig. 14 (a) shows the XRD pattern of FSM (flaxseed mucilage powder) and SPI (soya protein isolate). (b) shows XRD diffractogram of FSM alone and FSM + SPI-based scaffolds.

3.11 Drug release study

The antibacterial efficacy of ciprofloxacin-loaded scaffolds was assessed using the disc diffusion method against *Bacillus subtilis* (ATCC 168). Fig. 16 illustrates representative images of the zones of inhibition and provides a quantitative analysis of the antibacterial activity of various scaffold formulations compared with the Whatman filter paper control. All scaffold formulations exhibited measurable zones of inhibition, indicating successful drug loading and controlled ciprofloxacin release from the fabricated scaffolds. The control group (Whatman filter paper) displayed a zone of inhibition measuring 0.55 ± 0.05 cm, serving as the baseline for comparison. Among the FSM-only scaffolds, the zone of inhibition increased progressively with FSM concentration: 5% FSM (0.85 ± 0.05 cm), 6% FSM (0.9 cm), and 7% FSM (1.00 cm). This concentration-dependent enhancement suggests that higher FSM content facilitates improved drug retention and sustained release characteristics. The incorporation of 4% SPI into FSM scaffolds further enhanced antibacterial efficacy. The composite scaffolds demonstrated incrementally larger zones of inhibition: 5% FSM + 4% SPI (0.90 ± 0.10 cm), 6% FSM + 4% SPI (1.05 ± 0.05 cm), and 7% FSM + 4% SPI (1.1 ± 0.1 cm). The 7% FSM + 4% SPI formulation exhibited the maximum antibacterial activity with the largest zone of inhibition. The enhanced antibacterial performance of SPI-incorporated scaffolds can be attributed to the modified scaffold composition, porous architecture, and swelling behavior. The 7% FSM + 4% SPI formulation, with its optimized polymer network density, demonstrated the most effective drug retention and release profile, resulting in maximum bacterial growth inhibition. Conducting further investigations that directly quantify drug release concentrations would yield deeper insights into the correlation between scaffold composition and antibacterial efficacy.

4 Discussion

The current study successfully develops a fully plant-derived, extrusion-printable hydrogel system utilizing flaxseed mucilage (FSM) and soy protein isolate (SPI). The findings clearly demonstrate that the concentration of FSM and the incorporation of SPI are critical in determining the rheological behavior, printability, structural integrity, degradation, and physicochemical properties of the fabricated scaffolds. In this study, all inks exhibited shear-thinning behavior, with FSM–SPI blends showing a higher consistency index, a lower flow index, and a higher storage modulus than FSM alone. The blend of 7% FSM + 4% SPI exhibited the most robust, solid-like response and optimal filament fidelity. In comparison to other polysaccharide-based systems, such as psyllium Husk (PH)-gelatin blends, which exhibit a lower consistency index (49.30–530.59 Pa s) and higher tan δ values (0.5–1.05), the FSM–SPI inks demonstrate significantly higher consistency (660.09–3684.31 Pa s) and lower tan δ (0.35–0.55), indicating a more elastic, solid-like behavior. The flow index (n) values remain within a comparable shear-thinning range, while the yield stress of FSM–SPI inks (24.47–170.46 Pa) falls within the reported range for PH-gelatin systems (18.59–268.74 Pa), confirming their suitability for extrusion-based printing.[15] Similar patterns have been observed in plant protein–polysaccharide gel inks, where increasing polymer concentration and the addition of protein or polysaccharide co-components enhance yield stress and G', thereby improving 3D printability.[16] For instance, SPI-polysaccharide emulsion gels and SPI gels with apricot polysaccharides displayed higher viscosity, stronger shear-thinning, and improved printed line stability when the protein–polysaccharide network was reinforced, closely paralleling the behavior of the FSM–SPI blends in this study.[17] Methacrylated flaxseed-gum bioinks similarly required adequate solids and crosslinking to achieve robust, fatigue-resistant constructs, reinforcing the notion that tuning rheology through concentration and secondary components is crucial for flaxseed-derived inks.[18] Scanning electron microscopy (SEM) analysis indicated that an increased concentration of FSM led to denser walls and smaller pores, whereas the addition of SPI resulted in a more uniform, structurally reinforced pore network. After a 7 day immersion in PBS, the FSM with SPI scaffold showed greater weight loss. Similarly, reinforced flaxseed-mucilage/collagen aerogels exhibited comparable microstructural evolution; the incorporation of mucilage thickened the pore walls, enhanced interconnectivity, and improved resistance to collapse during degradation, thereby

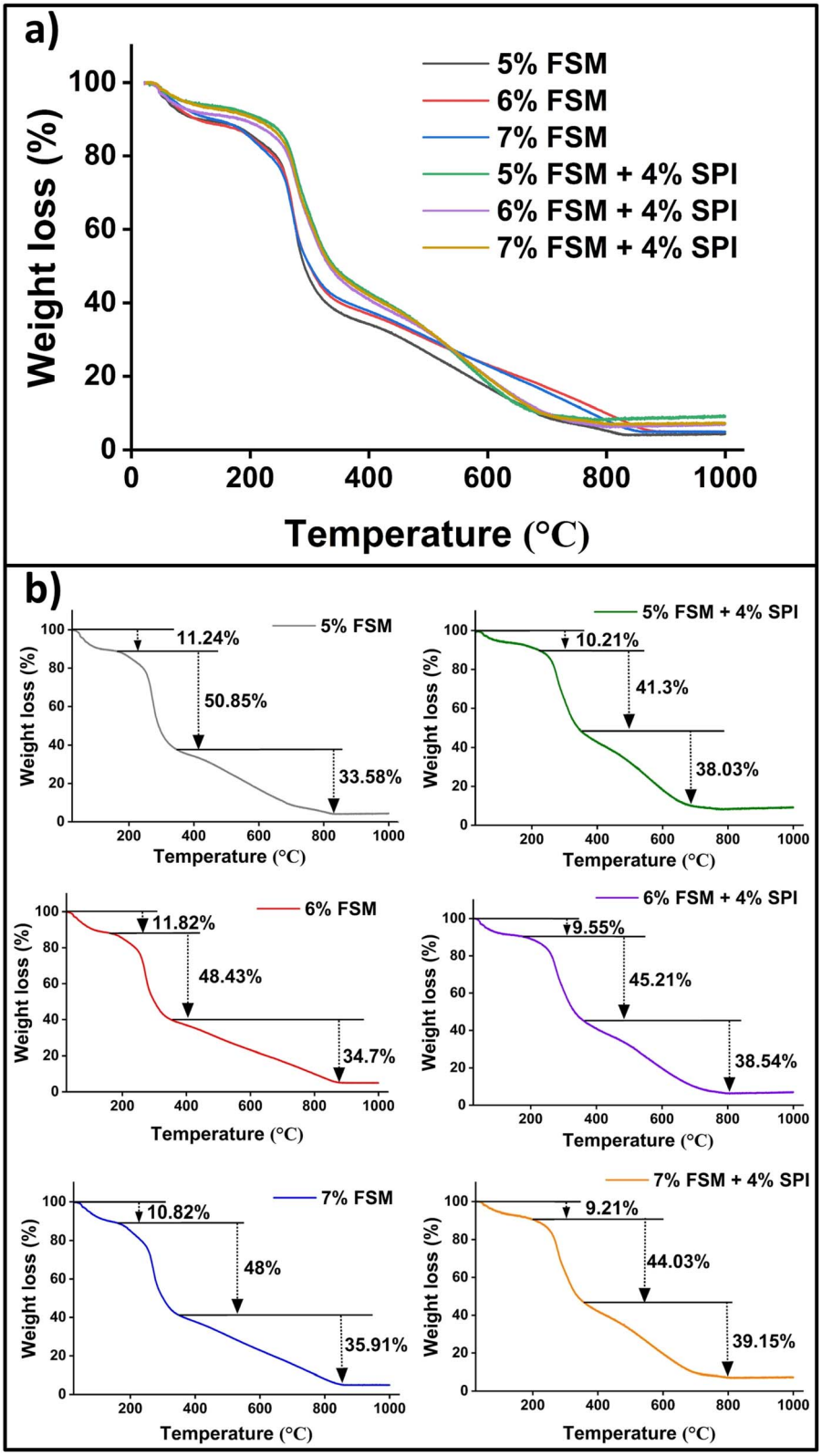

Fig. 15 (a) TGA plot of all fabricated scaffolds and (b) their individual graph showing weight loss at each stage.

leading to more stable three-dimensional architectures.[19,20] The pronounced swelling observed in pure FSM scaffolds and its reduction with increased FSM concentration and the addition of SPI align with the existing literature on flaxseed-mucilage cryogels and hydrogels, which are known to absorb hundreds to thousands of times their dry weight.[20] However, this swelling

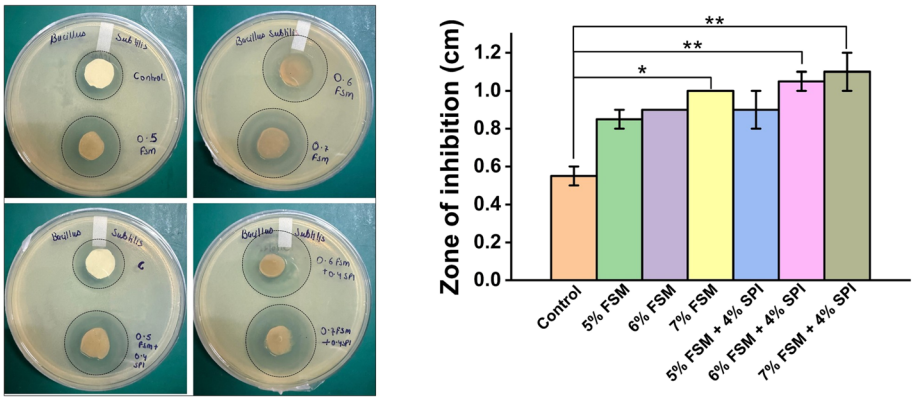

Fig. 16 Evaluation of the antibacterial drug release efficacy of FSM and FSM–SPI composite scaffolds against *Bacillus subtilis*. The figure includes a digital image and a quantitative analysis of the inhibition zone (cm) as determined by the disc diffusion assay.

can be reduced by increasing the polymer density or by adding additional crosslinkers. Similarly, SPI-polysaccharide hydrogels and SPI-dextran networks exhibit significant water uptake, which is counterbalanced by enhanced network cohesion.[21] This demonstrates that protein–polysaccharide interactions can simultaneously stabilize the scaffold and modulate swelling, consistent with the effects observed for SPI in the current system.

Under compression, the FSM and FSM–SPI scaffolds demonstrated moduli that increased with total solids, reaching their peak values at 7% FSM + 4% SPI while maintaining elastic recovery. Soy-protein hydrogels crosslinked with polysaccharides or oxidized dextran also exhibited a significant increase in modulus and fracture stress with higher crosslink density,[21] and FSM-reinforced collagen aerogels showed markedly improved stiffness compared to collagen alone,[20] paralleling the reinforcing role that SPI plays in the FSM matrix of this study. In addition, when compared to other plant-based hydrogels, such as aloe vera per cellulose nanofibril biohydrogels (compressive modulus: 0.92–6.54 kPa; compressive stress at 30% strain: 0.18–3.06 kPa), and xanthan gum/nanocellulose bioinks (compressive modulus: 5–15 kPa),[22] the FSM–SPI scaffolds investigated in this study demonstrate superior mechanical properties (compressive modulus: 10.86–24.96 kPa; compressive stress: 5.40–12.43 kPa).[23]

Fourier-transform infrared (FTIR) spectroscopy in this study confirmed the presence of characteristic polysaccharide bands for flaxseed mucilage (FSM) and the emergence of amide I/II peaks, along with shifted OH/carbonyl bands following the addition of SPI. Similar spectra, including broad OH bands, uronic acid and glycosidic vibrations, and emergent protein amide bands, have been documented for FSM-based films blended with elastin/collagen and for SPI-polysaccharide hydrogels.[24] The predominantly amorphous X-ray diffraction (XRD) patterns, characterized by diffuse halos and modest peaks around 16–25°, observed in this study are consistent with previous findings for flaxseed-gum films and FSM composites.[24] These exhibit broad features typical of amorphous hydrocolloids and slight peak sharpening or shifting when additional network formers enhance local chain packing rather than inducing true crystallinity. The thermogravimetric analysis (TGA) profiles of FSM and FSM–SPI hydrogels exhibited a characteristic three-stage degradation pattern. Initially, a moisture-release phase occurs below approximately 200 °C, followed by the significant decomposition of polysaccharide and protein chains between approximately 200 °C and 380 °C. These findings indicate that all formulations maintain thermal stability well above physiological and most processing temperatures, thereby affirming their potential as plant-based scaffolds for biomedical applications.[24]

The study on antibacterial drug release reveals that FSM and FSM–SPI composite scaffolds exhibit effective ciprofloxacin delivery, with concentration-dependent enhancement of antibacterial activity against *Bacillus subtilis*. The observed progressive increase in zones of inhibition with higher FSM concentrations suggests that increased polymer content facilitates improved drug retention and controlled release. The superior antibacterial performance at elevated FSM concentrations can be attributed to the increased polymer network density and enhanced entrapment efficiency.

5 Conclusion

This study establishes flaxseed mucilage as a viable polysaccharide platform for extrusion-printed hydrogels, demonstrating that co-formulation with soy protein isolate and EDC-NHS crosslinking results in scaffolds with enhanced rheological robustness, print fidelity, and structural stability. Increasing FSM concentration and incorporating 4% SPI systematically strengthen the gel network, enhance pore architecture, mitigate excessive swelling, and optimize thermal and compressive properties to suit soft-tissue scaffold applications. FTIR and XRD analyses confirm that these improvements arise from hydrogen-bond-mediated and covalent interactions, which organize the otherwise amorphous matrix into more compact, semi-ordered domains. As all components are plant-derived and processed in aqueous media, this system offers a sustainable alternative to animal-based or synthetic inks, providing a tunable platform for further functionalization with cells or therapeutic agents.

Author contributions

Pooja Kumari, conceptualization, writing – review & editing, writing original draft, methodology, data curation, Rishabh Rai Kaushik, methodology, data curation, Snehlata Yadav, methodology, data curation, Sanjeev Kumar Mahto, supervision, resource, investigation, formal analysis, validation.

Conflicts of interest

The author declares no conflict of interest.

Data availability

All data presented in this study were generated by the authors and are included within the manuscript.

Supplementary information (SI) is available. See DOI: https://doi.org/10.1039/d6ra00817h.

Acknowledgements

The authors would also like to sincerely acknowledge the support provided by the Central Instrument Facility, Indian Institute of Technology (Banaras Hindu University), for performing the characterization studies. Ms Pooja Kumari acknowledges the funding support for her scholarship received from the Department of Science and Technology, "Innovation in Science Pursuit for Inspired Research (INSPIRE)", Government of India.

References

1 M. Brovold, J. I. Almeida, I. Pla-Palacín, P. Sainz-Arnal, N. Sánchez-Romero, J. J. Rivas, H. Almeida, P. Royo Dachary, T. Serrano-Aulló, S. Soker and P. M. Baptista, *Adv. Exp. Med. Biol.*, 2018, **1077**, 421–449.
2 M. U. A. Khan, M. A. Aslam, M. F. B. Abdullah, W. S. Al-Arjan, G. M. Stojanovic and A. Hasan, *Arab. J. Chem.*, 2024, **17**, 105968.
3 S. Ramesh, O. L. A. Harrysson, P. K. Rao, A. Tamayol, D. R. Cormier, Y. Zhang and I. V. Rivero, *Bioprinting*, 2021, **21**, e00116.
4 F. Hernandez-Tenorio, E. Múnera-Gutiérrez, A. M. Miranda, A. A. Sáez, L. D. Marín-Palacio and C. Giraldo-Estrada, *Bioprinting*, 2025, **45**, e00383.
5 C.-A. Ghiorghita, I.-V. Platon, M. M. Lazar, M. V. Dinu and A. C. Aprotosoaie, *Carbohydr. Polym.*, 2024, **334**, 122033.
6 M. Kaur, R. Kaur and S. Punia, *Int. J. Biol. Macromol.*, 2018, **117**, 919–927.
7 J. Xu, M. Lou, Z. Wang, Q. Liu, Y. Yang, Z. Zhang, J. Wang, S. Zhang and H. Jin, *Int. J. Biol. Macromol.*, 2025, 149414.
8 H. Herrada-Manchón, M. A. Fernández and E. Aguilar, *Gels*, 2023, **9**(7), DOI: 10.3390/gels9070517.
9 P. H. E. N. de Paiva, L. G. Correa, A. F. S. Paulo, G. C. Balan, E. I. Ida and M. A. Shirai, *J. Food Sci. Technol.*, 2021, **58**, 3030–3038.
10 B. Safdar, Z. Pang, X. Liu, M. A. Jatoi and M. T. Rashid, *Int. J. Food Sci. Technol.*, 2020, **55**, 2481–2491.
11 B. Safdar, Z. Pang, X. Liu, M. A. Jatoi, A. Mehmood, M. T. Rashid, N. Ali and M. Naveed, *J. Food Biochem.*, 2019, **43**, e13014.
12 N. Varshney, P. Singh, R. Rai, N. K. Vishwakarma and S. K. Mahto, *Int. J. Biol. Macromol.*, 2023, **253**, 127268.
13 X. Ren, X. Meng, Z. Zhang, H. Du, T. Li and N. Wang, *Gels*, 2023, **9**(4), DOI: 10.3390/gels9040318.
14 S. Yan, Q. Wang, J. Yu, Y. Li and B. Qi, *Food Chem.:X*, 2023, **19**, 100866.
15 P. Agarwal, S. Poddar, N. Varshney, A. K. Sahi, K. Vajanthri, K. Yadav, A. Parmar and S. K. Mahto, *J. Biomater. Appl.*, 2021, **35**(9), 1132–1142.
16 O. Yildirim-Semerci, R. Onbas, R. Bilginer-Kartal and A. Arslan-Yildiz, *Innov. Emerg. Technol.*, 2024, **11**, 2440007.
17 K. Xu, C. Wu, G. Fan, X. Kou, X. Li, T. Li, J. Dou and Y. Zhou, *Int. J. Biol. Macromol.*, 2023, **242**, 124624.
18 K. Shu, Z. Huang, X. Pei, P. Y. M. Yew, S. Wei, Y. Yang, Y. Lan, D. Kai, L. Zheng and J. Zhao, *Composites, Part B*, 2023, **263**, 110864.
19 P. Kumari, K. M. Ahina, K. Kannan, S. Sreekumar, R. Lakra, U. T. Sivagnanam and M. S. Kiran, *Biomed. Mater.*, 2024, **19**, 025023.
20 P. Kumari, V. Vijayan, S. Sreekumar, R. Lakra, U. T. Sivagnanam and M. S. Kiran, *Mater. Today Commun.*, 2023, **34**, 105426.
21 J. Liu, Z. Li, Q. Lin, X. Jiang, J. Yao, Y. Yang, Z. Shao and X. Chen, *ACS Sustain. Chem. Eng.*, 2018, **6**, 13730–13738.
22 H. Baniasadi, E. Kimiaei, R. T. Polez, R. Ajdary, O. J. Rojas, M. Österberg and J. Seppälä, *Int. J. Biol. Macromol.*, 2022, **209**, 2020–2031.
23 H. Baniasadi, R. Ajdary, J. Trifol, O. J. Rojas and J. Seppälä, *Carbohydr. Polym.*, 2021, **266**, 118114.
24 G. Tewelde Hailu, F. Lemessa and M. Tesfaye Alemea, *Heliyon*, 2024, **10**, e35396.